

A Spatially Resolved Study of X-ray Properties in Superbubble 30 Dor C with *XMM – Newton*

YASUNORI BABAZAKI,<sup>1</sup> IKUYUKI MITSUISHI,<sup>1</sup> HIRONORI MATSUMOTO,<sup>2</sup> HIDETOSHI SANO,<sup>1</sup> YUMIKO YAMANE,<sup>1</sup>  
SATOSHI YOSHIIKE,<sup>1</sup> AND YASUO FUKUI<sup>1</sup>

<sup>1</sup>*Department of Physics, Nagoya University, Furo-cho, Chikusa-ku, Nagoya 464-8601, Japan*

<sup>2</sup>*Department of Earth and Space Science, Osaka University, Osaka 560-0043, Japan*

(Accepted July 27, 2018)

Submitted to ApJ

ABSTRACT

We carry out spatially resolved spectral analysis with a physical scale of  $\sim 10$  pc in X-ray for the superbubble 30 Dor C, which has the largest diameter of  $\sim 80$  pc and the brightest non-thermal emission in superbubbles for the first time. We aim at investigating spatial variation of the physical properties of non-thermal emission as detected in some supernova remnants in order to study particle acceleration in a superbubble. We demonstrated that non-thermal components are detected in all the regions covering the entire field of 30 Dor C. The spectra in the west region of 30 Dor C can be described with a combination of the thermal and non-thermal components while the spectra in the east region can be fitted with the non-thermal component alone. The photon index and absorption corrected intensity in 2–10 keV of the non-thermal component show spatial variation from  $\sim 2.0$  to  $\sim 3.7$  and  $(4\text{--}130) \times 10^{-8}$  erg s<sup>-1</sup> cm<sup>-2</sup> str<sup>-1</sup>, respectively, and the negative correlation between the non-thermal physical properties is observed. The temperature and normalization of the thermal component also vary within a range of  $\sim 0.2\text{--}0.3$  keV and  $\sim 0.2\text{--}7 \times 10^{17}$  cm<sup>-5</sup> str<sup>-1</sup>, respectively, and the positive correlation between the photon index and the normalization is also detected. We revealed the correlations in a superbubble for the first time as is the case in SNRs, which suggests the possibility that the same acceleration mechanism works also in the superbubble.

*Keywords:* X-rays: individual (30 Dor C) — X-rays: ISM — ISM: bubbles — acceleration of particles — individual objects (30 Dor C)

1. INTRODUCTION

X-ray and TeV gamma-ray observations clarify that supernova remnants (SNRs) are the acceleration sites of the cosmic rays up to the TeV range (e.g., [Koyama et al. 1995](#); [Ackermann et al. 2013](#)). The accelerated electrons with such energies emit non-thermal X-ray emission via synchrotron radiation which is characterized by power-law energy distribution in an X-ray band. Thus, understanding of the non-thermal properties in X-ray is of great importance to study the nature of the accelerated electrons.

The diffusive shock acceleration mechanism (e.g., [Zirakashvili & Ptuskin 2008](#)) is believed to be a relevant mechanism, which can explain the power-law spectrum of the non-thermal X-ray emission. Recently, it is reported that several SNRs exhibit the spatial shape variations of the non-thermal X-ray spectra with a physical scale of  $\sim 1\text{--}5$  pc (e.g., [Sano et al. 2015](#); [Tsubone et al. 2017](#)). Several authors (e.g., [Sano et al. 2015](#); [Tsubone et al. 2017](#)) suggest that the origin of the variations is due to the spatial difference of the cosmic-ray acceleration efficiency related to the surrounding interstellar gas distribution.

Superbubbles (SBs) are formed by combined phenomena of stellar winds from massive stars in OB associations and eventual supernovae (SNe) of those stars (e.g., [Bruhweiler et al. 1980](#)). The morphology of hot gas in SBs is

expected to be similar to that of a bubble blown by stellar winds of an isolated massive star (Weaver et al. 1977). The kinetic energy in some of SBs exceed that in a supernova ( $E_K \sim 10^{51}$  erg). SBs are filled with hot gas ( $\sim 10^6$  K) heated by stellar wind and SN ejecta. Non-thermal X-ray emission has been detected from a number of Galactic and extragalactic SBs, such as RCW38 (Wolk et al. 2002), Westerlund 1 (Muno et al. 2006), IC 131 (Tüllmann et al. 2009), N11 (Maddox et al. 2009), N51D (Cooper et al. 2004), and 30 Dor C (Bamba et al. 2004; Yamaguchi et al. 2009; Kavanagh et al. 2015), which suggests a potential accelerating power exceeding an SNR, even though the detection of the non-thermal emission in N11 and N51D is now doubtful due to the fluctuation of background point sources (Yamaguchi et al. 2010). However, very few studies have been performed to investigate the spatial variation of the non-thermal X-ray emission in the SBs and thus the cosmic-ray acceleration mechanism in the SBs has yet to be elucidated fully.

The SB, 30 Dor C, in Large Magellanic Cloud (LMC) was discovered by Le Marne (1968). It is believed that 30 Dor C has formed via stellar winds of the LH90 OB association (Testor et al. 1993) and several SNe. The SB has the strongest non-thermal X-ray emission among SBs and a large diameter of  $\sim 80$  pc. Thus, it is one of ideal laboratories for studying the non-thermal emission mechanisms associated with a SB. The SB includes not only the non-thermal emission but also the thermal emission from the shock-heated interstellar medium (e.g., Bamba et al. 2004; Yamaguchi et al. 2009; Kavanagh et al. 2015). Therefore, comparing the spatial distribution of the non-thermal and thermal emissions can provide us with hints to reveal association between the acceleration efficiency and the environment potentially. In this paper, we aim at investigating spatial variation of the physical properties in 30 Dor C with an unprecedented high resolution of  $\sim 10$  pc.

The paper is organized as follows: section 2 presents the observations of 30 Dor C with *XMM – newton* and the data reduction, and sections 3 and 4 describe our analysis method and the results, and the discussions on the spatial variation of the physical properties, respectively. In section 5, we summarize our results and discussions. At 30 Dor C assuming a distance of  $\sim 50$  kpc to the LMC,  $1'$  corresponds to 15 pc. In this paper, we used HEASoft v6.21, XSPEC version 12.9, the *XMM – Newton* Source Analysis Software (XMM-SAS) packaged in SAS 15.0.0 for our spectral analysis and a metal-abundance table tabulated in Anders & Grevesse (1989). Unless otherwise stated, the error ranges show the 90% confidence level from the center value.

## 2. OBSERVATION AND DATA REDUCTION

We, first, retrieved all of the data available for 30 Dor C in the *XMM – Newton* Science Archive, and then selected the data taken from the pn instrument in European Photon Image Camera (EPIC, Jansen et al. 2001) with rich ( $> 50$  ks) net exposure time after the removal of the background flare periods to take advantage of the larger effective area than those of the EPIC-MOS instrument and avoid the systematic error between the detectors.

The basic information of the observations is shown in Table 1. We generated calibrated event files with the SAS tools `epchain`. Time intervals with high background rates ( $> 0.4$  cts) seen in light curves of an off-source region in

**Table 1.** Observation Log for 30 Dor C

Obs. ID	R.A.	Dec.	Date	Exposure (ks) <sup>a</sup>
	(J2000.0)	(J2000.0)		pn
0104660101	05h35m27.99s	-69d16m11.0s	2000 Nov. 17	3
0406840301	05h35m27.99s	-69d16m11.1s	2007 Jan. 1	63
0506220101	05h35m28.30s	-69d16m13.0s	2008 Jan. 11	68
0556350101	05h35m28.30s	-69d16m13.0s	2009 Jan. 30	63
0601200101	05h35m28.30s	-69d16m13.0s	2009 Dec. 11	71
0650420101	05h35m28.30s	-69d16m13.0s	2010 Dec. 12	51
0671080101	05h35m28.30s	-69d16m13.0s	2011 Dec. 02	61
0690510101	05h35m28.30s	-69d16m13.0s	2012 Dec. 11	60

<sup>a</sup>All exposure times show flare-filtered exposure times.

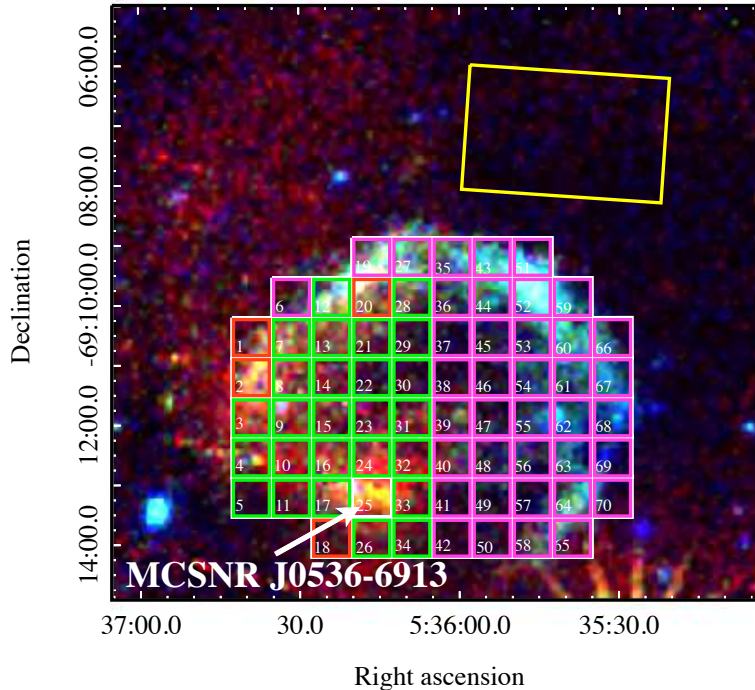


**Figure 1.** *XMM – Newton* EPIC-pn image of 30 Dor C in 0.3–1 keV (red), 1–2 keV (green), and 2–7 keV (blue), respectively. Spectra were extracted from the square regions ( $\sim 0.7 \times 0.7$ ) with a region number. One- (non-thermal), two- (one-temperature and non-thermal), and three-component (two-temperature and non-thermal) models are finally adopted in magenta-, green-, and red-color box regions. The background spectrum was extracted from the yellow rectangle.

10–12 keV were discarded in each observation. The event lists were then filtered further, keeping only 0-4 patterns in an energy range of 0.4–12 keV.

### 3. ANALYSIS AND RESULTS

In order to conduct spatially detailed X-ray spectral analysis for 30 Dor C, spectrum for each region is extracted from all the seven data and the extracted spectra are fitted simultaneously to reduce the statistical error. Each spectrum is rebinned to have at least 25 counts per an energy bin to allow the use of the  $\chi^2$ -statistic. The energy range in 0.5–7 keV was used in our analysis to avoid detector noise and the EPIC-pn fluorescence line forest just above 7 keV. The SAS tasks `rmfgen` and `arfgen` were utilized to create redistributed matrix files (RMF) and ancillary response files (ARF) respectively.

#### 3.1. X-ray Background Evaluation

Firstly, we selected a source-free area in the vicinity of 30 Dor C to reduce spatial variation of the detector noise in the field of view shown in figure 1 as a background region. Then, we conducted spectral analysis to confirm whether the region is suitable or not as a background region. In order to create quiescent particle background (QPB) spectra, we used *XMM – Newton* Extended Source Analysis Software (XMM-ESAS), packaged in SAS 15.0.0. The QPB spectra were subtracted from the spectrum of each region in each observation.

For our spectral analysis, we used the following physically motivated model:

$$(apec_{\text{LHB}} + phabs_{\text{Galaxy}} * (apec_{\text{GH}} + vphabs_{\text{LMC}} * (powerlaw_{\text{CXB}})))$$

The X-ray background emission is comprised of three components (e.g., Yoshino et al. 2009), such as an unabsorbed thermal ( $kT \sim 0.1$  keV) emission from the Local Hot Bubble (LHB), an absorbed thermal ( $kT \sim 0.2$ – $0.3$  keV) emission from the Galactic halo (GH), and an absorbed powerlaw ( $\Gamma = 1.4$ , see Kushino et al. 2002) which is known as cosmic

X-ray background (CXB). We used collisionally-ionized optically-thin thermal plasma model APEC (Smith et al. 2001) for the LHB and GH in XSPEC. The metal abundance of these models is fixed to a solar abundance. Because the temperature of the LHB component was not constrained well, the temperature is fixed to be a typical value of 0.1 keV (Yoshino et al. 2009). The absorption by our Galaxy and the LMC was also taken into account. We used a photo-electric absorption model in XSPEC, namely phabs, as the Galactic absorption model. The column density  $N_{\text{H}}$  was fixed at  $6 \times 10^{20} \text{ cm}^{-2}$  (Dickey & Lockman 1990) in the direction of 30 Dor C, assuming the solar abundance. The absorption by the LMC is modeled with vphabs, in which we can set each metal abundance separately. The metal abundance was fixed to the representative LMC values ( $\text{C}=0.30 Z_{\odot}$ ,  $\text{O}=0.26 Z_{\odot}$ ,  $\text{Ne}=0.33 Z_{\odot}$ , Russell & Dopita 1992; Someya et al. 2014), while the absorption column density is set to be free. The background spectrum, however, can not be described with the model above and there is a significant residual feature around  $\sim 1$  keV corresponding to emission lines from complex Fe L. We hence added another thermal component,  $\text{apec}_{\text{LMC}}$ , with a different temperature as follows:

$$(apec_{\text{LHB}} + phabs_{\text{Galaxy}} * (apec_{\text{GH}} + vphabs_{\text{LMC}} * (apec_{\text{LMC}} + powerlaw_{\text{CXB}})).$$

The fitting results improved significantly and the spectrum with the best-fit model is shown in figure 2. The best-fit parameters are summarized in Table 2. The plasma temperature of the added thermal component is consistent with that of the ISM in the LMC (e.g., Sasaki et al. 2002). The 2–10 keV surface brightness of the power-law component was

**Table 2.** Best fit parameters obtained by using all seven observations for the background region

Component	Parameter	Best-fit Value
Absorption		
Galactic (phabs)	$N_{\text{H,Gal}}$	0.06 (fixed) <sup>a</sup>
LMC (vphabs) <sup>b</sup>	$N_{\text{H,LMC}}$	$0.20 \pm 0.16$
Astrophysical X-ray Forground and Background		
LHB (apec) <sup>c</sup>	$kT$ (keV)	0.1 (fixed) <sup>d</sup>
	$Norm$ <sup>e</sup>	<12
GH (apec) <sup>c</sup>	$kT$ (keV)	$0.22 \pm 0.01$
	$Norm$ <sup>e</sup>	$42.5^{+4.0}_{-4.8}$
CXB (powerlaw)	$\Gamma$	1.4 (fixed) <sup>f</sup>
	2-10 keV intensity <sup>g</sup>	$6.0 \pm 1.3$
Thermal emission in LMC		
ISM (vapec) <sup>b</sup>	$kT$ (keV)	$0.89^{+0.04}_{-0.03}$
	$Norm$ <sup>e</sup>	$83^{+17}_{-15}$
	$\chi^2/d.o.f$	509/375

<sup>a</sup>Fixed to the Galactic column density from the HI maps (Dickey & Lockman 1990). The unit is  $10^{22} \text{ cm}^{-2}$ .

<sup>b</sup>Fixed to the representative LMC values (Russell & Dopita 1992; Someya et al. 2014).

<sup>c</sup>Fixed to a solar abundance table tabulated in Anders & Grevesse (1989).

<sup>d</sup>Fixed to the value derived from Yoshino et al. (2009).

<sup>e</sup>Normalization of the apec model divided by a solid angle  $\Omega$ .  $Norm = (1/\Omega) n_e n_{\text{H}} dV / [4((1+z)D_A)^2]$  in unit of  $10^{14} \text{ cm}^5 \text{ str}^{-1}$ , where,  $z$ ,  $n_e$ ,  $n_{\text{H}}$ ,  $D_A$ , and  $V$  are the redshift, the electron and hydrogen number densities ( $\text{cm}^{-3}$ ), the angular diameter distance (cm) and the emission volume ( $\text{cm}^3$ ), respectively.

<sup>f</sup>Fixed to an averaged value derived in Kushino et al. (2002).

<sup>g</sup>The unit is  $10^{-8} \text{ erg s}^{-1} \text{ cm}^{-2} \text{ str}^{-1}$ .

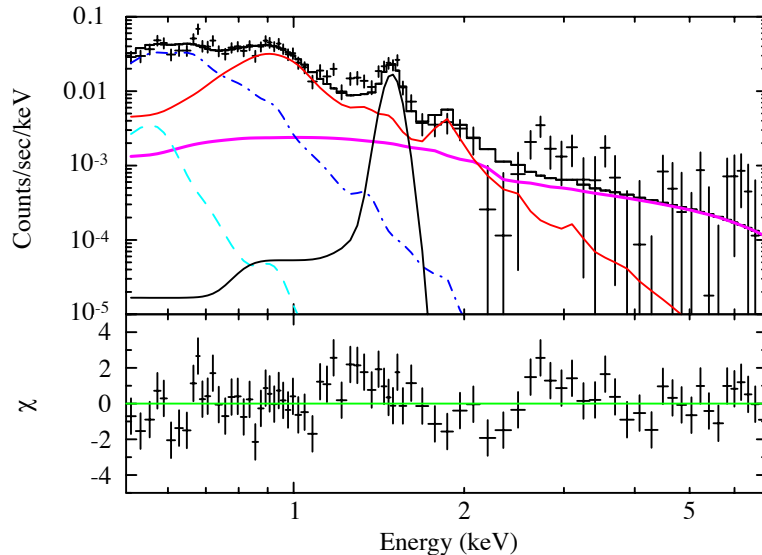


**Figure 2.** A representative spectrum of a background region (Obs. ID: 0601200101) with the best-fit model. The dashed (cyan), dashed-dotted (blue), bold (magenta), solid (red) and solid (black) lines show the LHB, GH, CXB, ISM in the LMC and an artificial Al line, respectively.

$(6.0 \pm 1.3) \times 10^{-8} \text{ erg s}^{-1} \text{ cm}^{-2} \text{ str}^{-1}$  and the value is in good agreement with the expected CXB intensity (Kushino et al. 2002). We confirmed that the best fit parameters are consistent with those obtained in each observation and thus all the spectra were fitted simultaneously to reduce the statistical error. Any further components such as a soft proton model are not required. Thus, we concluded that the region and model are appropriate to evaluate the X-ray background components including the ISM of the LMC in our analysis.

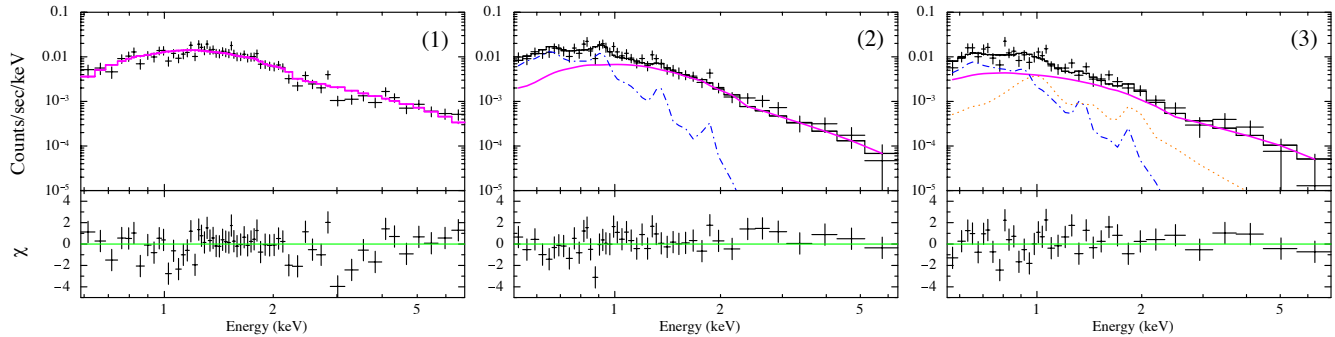


**Figure 3.** Examples of the spectra with the best-fit non-thermal-, two-, and three-, component models. (1) non-thermal-component model for the spectrum in region 52. (2) two-component model for the spectrum in region 13. (3) three-component model for the spectrum in region 1. The magenta solid, blue dashed-dotted and orange dotted lines show non-thermal, low-temperature and high-temperature components, respectively. The spectra are extracted from obsid 0601200101.

### 3.2. Spectral Analysis for the 30 Dor C Field

In order to investigate spatial variation of the non-thermal X-ray emission in 30 Dor C, we divided the 30 Dor C region into 70 regions of  $10 \text{ pc} \times 10 \text{ pc}$  ( $0.7 \times 0.7$ ) grids in unprecedented detail. The region number is shown in figure 1. In our spectral analysis, the background spectrum defined in §3.1 was subtracted from each region in each observation.

As indicated in previous studies (e.g., Bamba et al. 2004; Yamaguchi et al. 2009; Kavanagh et al. 2015), not only non-thermal emission but also thermal emission is sometimes required at the same time to explain the observed spectra. Actually, some spectra show significant enhancement around 0.6 and/or 1 keV corresponding to emission

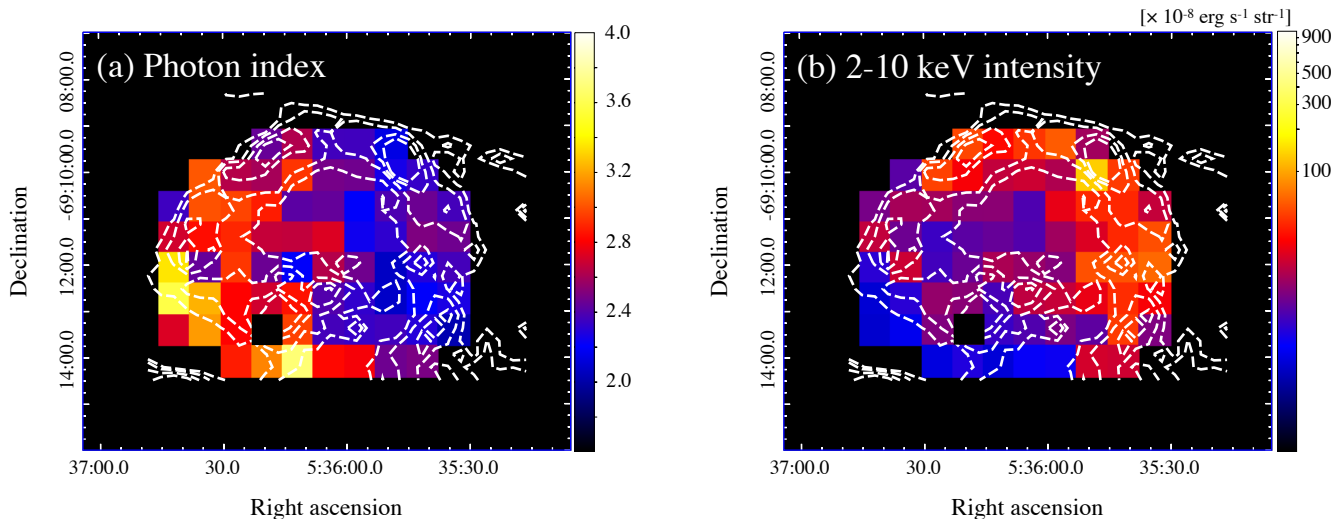


**Figure 4.** Maps of the best-fit parameters: (a) the photon index  $\Gamma$  and (b) absorption-corrected intensity in 2–10 keV [ $10^{-8} \text{ erg s}^{-1} \text{ cm}^{-2} \text{ str}^{-1}$ ], of the non-thermal component. Smoothed white contours of the *XMM-Newton* EPIC-pn images (0.5–7 keV) are overlaid in the maps.

lines of highly-ionized oxygen / Fe L-shell complex, respectively. We attempted to apply three models in the following order, (1) non-thermal model, (2) two-component (non-thermal and one-temperature thermal) model, and (3) three-component (non-thermal and two-temperature thermal) model. For regions where the fit significantly ( $\geq 99\%$  in an F test) improved by adding an additional thermal component, we adopted the two- or three-component model. A collisionally-ionized optically-thin thermal plasma model, APEC, was used also for the thermal plasma in the regions except a young SNR, MCSNR J0536-6913, associated with 30 Dor (see the region number 25 in figure 1). The metal abundance of the low- / high-temperature plasmas mainly emitting oxygen / Fe L-shell lines is fixed to those reported in Yamaguchi et al. (2009) / Russell & Dopita (1992). The intrinsic absorption column density in the LMC is applied for the both plasmas and linked to that of the non-thermal model. The only spectrum around MCSNR J0536-6913 was well expressed with a combination of the non-thermal and non-equilibrium ionization collisional plasma models due to a heavy contamination from the SNR as shown in Kavanagh et al. (2015) and thus we removed the results in our discussion.

Most of the spectra in the east region can be well described with the two- or three-component model, whereas most of the spectra in the west region can be well fitted with the non-thermal-component model as shown in Figure 1. Figure 3 shows examples of the spectra with the best-fit non-thermal-, two-, and three-component models. We investigated the photon index and intensity of the non-thermal component, the temperature and intensity of the thermal component, and the intrinsic absorption column density of the LMC. The best-fit parameters in the best fit model are summarized in Table 3.

Figures 4 (a) and (b) show the distributions of the photon index and absorption corrected 2–10 keV intensity of the non-thermal component, respectively. It is found for the first time that the non-thermal component is detected significantly in all the 70 regions covering the entire region of 30 Dor C. Their typical relative error is  $\sim 8\%$ . The photon index shows spatial variation of  $\sim 2.0$ – $3.7$ . The areas with the relatively steep / flat photon indices are distributed in the east / west regions, respectively. Even though this sort of high spatial resolution spectral analysis had not been performed so far, the trend is consistent with the previous studies (e.g., Kavanagh et al. 2015). The intensity in 2–10 keV significantly varies by more than an order of magnitude ( $\sim 4$ – $130 \times 10^{-8} \text{ erg s}^{-1} \text{ cm}^{-2} \text{ str}^{-1}$ ) in the field and is relatively large in the west region of the shell structure. Their typical relative error is  $\sim 15\%$ .

The temperature and normalization of the thermal component mainly emitting oxygen lines vary from  $\sim 0.2$  to  $\sim 0.3$  keV and from  $\sim 0.2$  to  $\sim 7 [10^{17} \text{ cm}^{-5} \text{ str}^{-1}]$ , respectively. Because the low-temperature thermal plasma is not detected in the source-free region of the vicinity of 30 Dor C and the morphology apparently forms a shell-like structure as shown in figure 1, the plasma may be associated with 30 Dor C. Such low-temperature plasma with a temperature of  $\sim 0.1$ – $0.3$  keV is found also in other SBs (e.g., Dunne et al. 2001; Yamaguchi et al. 2010) and detected mainly in the east region as previously reported in Bamba et al. (2004); Yamaguchi et al. (2009); Kavanagh et al. (2015). The

temperature and normalization of the thermal component mainly emitting Fe L-shell lines vary from  $\sim 0.9$  to  $\sim 1.2$  keV and from  $\sim 0.1$  to  $\sim 0.2$  [ $10^{17}$  cm $^{-5}$  str $^{-1}$ ], respectively. The temperature is consistent with that of the observed in the source-free region within the statistical error. According to the results of [Sasaki et al. \(2002\)](#), the flux of ISM in LMC varies by more than twice depending on the regions. The normalization of the high-temperature components is consistent with that of the observed in background spectra within the variation. While the results suggest that the high-temperature plasma may be due to the spatial variation of the ISM in the LMC, the origin of the component is beyond our scope. We confirmed that the uncertainty, e.g., in the metal abundance, does not affect our results for the non-thermal component significantly.

The intrinsic absorbing column density  $N_{\text{H}}$  of the LMC ranges from  $\sim 0.3$  to  $\sim 2 \times 10^{22}$  cm $^{-2}$  and a typical relative error is  $\sim 15$  %. The intrinsic absorption in the east area of 30 Dor C seems to be relatively small ( $\sim 0.6 \times 10^{22}$  cm $^{-2}$ ) while large ( $\sim 1 \times 10^{22}$  cm $^{-2}$ ) in the west of the shell-like structure.

We confirmed that our representative results for our spectral analysis on the temperature of the thermal components, photon index of the non-thermal components, and intrinsic absorbing column density in the LMC are consistent with those of the previous studies (e.g., [Bamba et al. 2004](#); [Smith & Wang 2004](#); [Yamaguchi et al. 2009](#); [Kavanagh et al. 2015](#)).

#### 4. DISCUSSION

We conducted the spatially resolved spectral analysis of 30 Dor C with a physical scale of  $\sim 10$  pc in X-ray for the first time. We revealed that the non-thermal emission exists in all the regions covering the whole area of 30 Dor C and extracted the distribution of the physical properties such as the photon index and absorption-corrected intensity of the non-thermal component. We found that the spectral shape changes and therefore the physical properties vary in this field. In this section, we discussed, in particular, the origin of the spatial variation of the non-thermal X-ray properties to study the mechanism of cosmic-ray acceleration in SBs.

Some SNRs also show spatial variation of the photon index and intensity of the non-thermal component (e.g., [Sano et al. 2015](#); [Tsubone et al. 2017](#)). In particular, pc-scale spatially resolved spectral analysis reveals that the photon index closely correlates with the synchrotron X-ray intensity (e.g., [Sano et al. 2015](#)). Thus, we also extracted the relation between the photon index and the synchrotron X-ray intensity in the same manner as shown in figure 5(a). There is a clear negative correlation with a correlation coefficient of  $\sim -0.5$ . One of the interpretations is due to a shock-cloud interaction. Magnetohydrodynamic numerical simulations in [Inoue et al. \(2012\)](#) predict that such spatial variation can be produced by the shock-cloud interaction because the synchrotron X-ray intensity is positively correlated with the strength of the enhanced magnetic field due to the turbulence occurred in the interaction. The photon index also can be changed by the enhanced magnetic field since the particle acceleration occurs efficiently. Therefore, it is naturally expected that the photon index gets flatter with increasing the synchrotron X-ray intensity.

According to the scenario, the larger the photon index is, the smaller the cut-off energy in the energy distribution of electrons should be. When we applied a broken power-law model instead of the power-law model for the non-thermal X-ray emission, however, no constraint was given to the breaking energy with the X-ray spectra alone. The correlation between the photon index and the cut-off energy has been observed in some SNRs when X-ray synchrotron spectra are analyzed using the SRCUT model ([Reynolds 1998](#); [Reynolds & Keohane 1999](#)) combined with radio synchrotron spectra ([Rothenflug et al. 2004](#); [Bamba et al. 2005a,b](#)). The spatially-resolved flux and spectral index of the radio synchrotron emission of 30 Dor C have been obtained in [Kavanagh et al. \(2015\)](#), but as the authors say it is difficult to obtain their reliable values for the entire region of 30 Dor C due to the contaminations of a foreground molecular cloud and of thermal radio emission. This situation prevents us from analyzing the multi-wavelength spectra from radio to X-ray. The analysis of the spatially-resolved spectral energy distribution is left to future works.

[Sano et al. \(2017\)](#) presents the molecular cloud distribution around 30 Dor C and it seems that there is a positive correlation between the synchrotron X-ray intensity and the amount of the molecular cloud. The detailed comparison between X-ray and radio observations will be discussed ([Yamane et al. in prep.](#)).

[Tsubone et al. \(2017\)](#) argues that efficient acceleration occurs in the low density environment implying that the photon index steepens with increasing the normalization of the thermal component observationally based on the pc-scale spectral analysis results. Thus, we also extracted the relation as shown in figure 5(b). One can see a positive correlation with a correlation coefficient of  $\sim 0.4$  and thus similarities for SNRs are found in terms of the correlations between the non-thermal properties themselves and the non-thermal and thermal properties, which suggests the possibility that the same acceleration mechanism works also in the superbubble.

The bright non-thermal X-ray emission in 30 Dor C was detected. However, no other SBs exhibit such a bright non-thermal emission. The SBs, where non-thermal X-ray emission has been significantly detected, are only RCW38

**Table 3.** Best fit parameters of fitting .

Region num.	LMC absorption	Power-law component		Low temperature component		High temperature component		$\chi^2/d.o.f$
	$N_{H,LMC}^a$	$\Gamma$	2-10 keV intensity <sup>b</sup>	$kT^c$	$Norm^d$	$kT^c$	$Norm^d$	
1	$0.26^{+0.20}_{-0.12}$	$2.35^{+0.29}_{-0.29}$	$12.6^{+2.8}_{-2.6}$	$0.26^{+0.03}_{-0.04}$	$0.62^{+0.94}_{-0.27}$	$1.09^{+0.18}_{-0.06}$	$0.12^{+0.06}_{-0.05}$	244/211
2	$0.37^{+0.12}_{-0.11}$	$2.69^{+0.19}_{-0.19}$	$21.0^{+3.2}_{-3.5}$	$0.25^{+0.03}_{-0.03}$	$1.65^{+1.3}_{-0.75}$	$1.19^{+0.41}_{-0.25}$	$0.14^{+0.10}_{-0.08}$	253/300
3	$0.47^{+0.10}_{-0.11}$	$3.34^{+0.16}_{-0.29}$	$7.5^{+1.6}_{-1.4}$	$0.23^{+0.03}_{-0.02}$	$2.7^{+1.8}_{-1.0}$	—	—	255/268
4	$0.54^{+0.18}_{-0.12}$	$3.57^{+0.43}_{-0.42}$	$4.2^{+1.5}_{-1.1}$	$0.23^{+0.03}_{-0.04}$	$2.7^{+4.2}_{-1.1}$	—	—	160/160
5	$0.56^{+0.27}_{-0.22}$	$2.72^{+0.66}_{-0.62}$	$4.1^{+2.2}_{-1.6}$	$0.24^{+0.05}_{-0.05}$	$1.24^{+2.9}_{-0.74}$	—	—	98/127
6	$0.33^{+0.08}_{-0.08}$	$3.01^{+0.21}_{-0.19}$	$10.3^{+2.0}_{-1.8}$	—	—	—	—	174/162
7	$0.68^{+0.10}_{-0.11}$	$2.99^{+0.15}_{-0.14}$	$17.3^{+2.2}_{-2.1}$	$0.19^{+0.02}_{-0.01}$	$5.7^{+4.0}_{-2.7}$	—	—	271/274
8	$0.60^{+0.20}_{-0.11}$	$2.83^{+0.25}_{-0.23}$	$11.8^{+2.2}_{-2.0}$	$0.23^{+0.02}_{-0.04}$	$3.5^{+5.6}_{-1.3}$	—	—	254/249
9	$0.50^{+0.23}_{-0.13}$	$2.44^{+0.23}_{-0.16}$	$22.4^{+3.4}_{-3.0}$	$0.23^{+0.02}_{-0.04}$	$2.3^{+5.1}_{-1.0}$	—	—	281/235
10	$0.63^{+0.11}_{-0.12}$	$3.22^{+0.35}_{-0.33}$	$7.4^{+2.1}_{-1.7}$	$0.19^{+0.02}_{-0.01}$	$7.2^{+4.6}_{-3.2}$	—	—	185/177
11	$0.35^{+0.12}_{-0.15}$	$3.17^{+0.35}_{-0.33}$	$5.0^{+1.5}_{-1.2}$	$0.25^{+0.05}_{-0.02}$	$1.19^{+0.86}_{-0.62}$	—	—	183/193
12	$0.58^{+0.13}_{-0.13}$	$2.63^{+0.10}_{-0.10}$	$49.5^{+4.1}_{-3.9}$	$0.19^{+0.05}_{-0.02}$	$2.0^{+2.9}_{-1.6}$	—	—	380/369
13	$0.74^{+0.10}_{-0.11}$	$2.96^{+0.17}_{-0.16}$	$17.0^{+2.5}_{-2.2}$	$0.19^{+0.02}_{-0.01}$	$7.4^{+4.8}_{-3.3}$	—	—	239/251
14	$0.50^{+0.26}_{-0.16}$	$2.89^{+0.37}_{-0.26}$	$8.4^{+1.9}_{-1.6}$	$0.23^{+0.04}_{-0.05}$	$1.71^{+4.7}_{-0.92}$	—	—	198/185
15	$0.53^{+0.22}_{-0.16}$	$2.93^{+0.38}_{-0.31}$	$8.8^{+2.4}_{-2.0}$	$0.23^{+0.03}_{-0.04}$	$2.3^{+4.4}_{-1.2}$	—	—	172/172
16	$0.53^{+0.10}_{-0.13}$	$2.80^{+0.17}_{-0.16}$	$15.5^{+2.2}_{-2.1}$	$0.21^{+0.03}_{-0.02}$	$4.1^{+3.0}_{-1.9}$	—	—	271/249
17	$0.41^{+0.17}_{-0.08}$	$2.80^{+0.17}_{-0.17}$	$13.4^{+1.9}_{-1.7}$	$0.23^{+0.02}_{-0.01}$	$2.68^{+0.98}_{-0.79}$	—	—	359/315
18	$0.29^{+0.24}_{-0.20}$	$2.87^{+0.51}_{-0.48}$	$4.5^{+1.8}_{-1.5}$	$0.23^{+0.06}_{-0.04}$	$0.64^{+1.5}_{-0.44}$	$0.93^{+0.19}_{-0.15}$	$0.11^{+0.04}_{-0.04}$	163/156
19	$0.35^{+0.05}_{-0.04}$	$2.44^{+0.09}_{-0.08}$	$50.9^{+4.6}_{-4.3}$	—	—	—	—	293/291
20	$0.51^{+0.19}_{-0.19}$	$2.59^{+0.16}_{-0.16}$	$30.3^{+3.4}_{-3.2}$	$0.19^{+0.03}_{-0.02}$	$2.5^{+4.1}_{-1.9}$	$0.95^{+0.26}_{-0.15}$	$0.22^{+0.07}_{-0.08}$	321/317
21	$0.80^{+0.14}_{-0.25}$	$2.86^{+0.20}_{-0.19}$	$14.4^{+2.5}_{-2.2}$	$0.19^{+0.05}_{-0.01}$	$5.1^{+3.8}_{-3.8}$	—	—	222/214
22	$0.94^{+0.20}_{-0.36}$	$2.66^{+0.29}_{-0.27}$	$10.4^{+2.7}_{-2.3}$	$0.19^{+0.08}_{-0.04}$	$4.2^{+11}_{-3.4}$	—	—	133/125
23	$0.24^{+0.19}_{-0.10}$	$2.45^{+0.25}_{-0.23}$	$11.6^{+2.6}_{-2.2}$	$0.30^{+0.05}_{-0.06}$	$0.47^{+0.67}_{-0.20}$	—	—	209/187
24	$0.32^{+0.10}_{-0.11}$	$2.69^{+0.17}_{-0.16}$	$14.3^{+2.2}_{-2.0}$	$0.19^{+0.01}_{-0.01}$	$4.4^{+2.7}_{-1.9}$	—	—	289/277
25 <sup>e</sup>	—	—	—	—	—	—	—	—
26	$0.44^{+0.11}_{-0.14}$	$3.11^{+0.26}_{-0.25}$	$7.0^{+1.5}_{-1.3}$	$0.24^{+0.04}_{-0.02}$	$1.53^{+1.0}_{-0.76}$	—	—	233/210
27	$0.42^{+0.06}_{-0.05}$	$2.62^{+0.10}_{-0.10}$	$33.1^{+3.8}_{-3.5}$	—	—	—	—	260/258
28	$0.78^{+0.14}_{-0.19}$	$2.92^{+0.08}_{-0.18}$	$21.2^{+3.2}_{-2.9}$	$0.17^{+0.03}_{-0.02}$	$6.0^{+7.8}_{-4.1}$	—	—	212/207
29	$0.82^{+0.28}_{-0.39}$	$2.41^{+0.24}_{-0.22}$	$14.6^{+3.3}_{-2.9}$	$0.19^{+0.07}_{-0.04}$	$3.1^{+16}_{-2.7}$	—	—	112/128
30	$0.91^{+0.30}_{-0.37}$	$2.66^{+0.30}_{-0.24}$	$11.3^{+2.6}_{-2.2}$	$0.18^{+0.07}_{-0.05}$	$4.2^{+26}_{-3.6}$	—	—	149/146
31	$0.32^{+0.15}_{-0.14}$	$2.19^{+0.22}_{-0.21}$	$18.0^{+3.2}_{-2.9}$	$0.30^{+0.05}_{-0.04}$	$0.83^{+0.68}_{-0.38}$	—	—	153/188
32	$0.49^{+0.11}_{-0.12}$	$2.84^{+0.26}_{-0.25}$	$9.1^{+2.1}_{-1.8}$	$0.19^{+0.02}_{-0.01}$	$4.4^{+3.1}_{-2.1}$	—	—	250/207
33	$0.47^{+0.10}_{-0.18}$	$2.96^{+0.23}_{-0.22}$	$8.3^{+1.7}_{-1.4}$	$0.20^{+0.04}_{-0.01}$	$3.6^{+2.3}_{-2.0}$	—	—	245/249
34	$0.73^{+0.13}_{-0.14}$	$3.68^{+0.37}_{-0.37}$	$4.3^{+1.2}_{-1.0}$	$0.18^{+0.02}_{-0.02}$	$4.5^{+5.4}_{-2.5}$	—	—	211/166
35	$0.49^{+0.07}_{-0.07}$	$2.35^{+0.11}_{-0.11}$	$45.6^{+5.0}_{-4.7}$	—	—	—	—	193/209
36	$0.52^{+0.09}_{-0.08}$	$2.48^{+0.15}_{-0.14}$	$22.5^{+3.3}_{-3.1}$	—	—	—	—	177/152
37	$0.57^{+0.15}_{-0.13}$	$2.44^{+0.23}_{-0.21}$	$9.6^{+3.4}_{-3.0}$	—	—	—	—	126/117
38	$0.58^{+0.13}_{-0.12}$	$2.72^{+0.23}_{-0.21}$	$9.8^{+2.2}_{-1.9}$	—	—	—	—	145/138
39	$0.82^{+0.26}_{-0.21}$	$2.63^{+0.25}_{-0.19}$	$15.7^{+2.6}_{-2.3}$	$0.24^{+0.05}_{-0.05}$	$2.2^{+6.2}_{-1.4}$	—	—	185/186
40	$0.46^{+0.20}_{-0.19}$	$2.39^{+0.16}_{-0.17}$	$20.5^{+2.9}_{-2.7}$	$0.21^{+0.04}_{-0.03}$	$1.4^{+2.6}_{-0.9}$	—	—	170/187

**Table 3.** Best fit parameters of fitting .

Region num.	LMC absorption	Power-law component		Low temperature component		High temperature component		$\chi^2/d.o.f$
	$N_{H,LMC}^a$	$\Gamma$	2-10 keV intensity <sup>b</sup>	$kT^c$	$Norm^d$	$kT^c$	$Norm^d$	
41	$0.34_{-0.15}^{+0.35}$	$2.36_{-0.23}^{+0.24}$	$9.7_{-1.9}^{+2.2}$	$0.33_{-0.11}^{+0.16}$	$0.21_{-0.14}^{+0.92}$	—	—	184/156
42	$0.33_{-0.10}^{+0.11}$	$2.82_{-0.24}^{+0.27}$	$5.9_{-1.3}^{+1.5}$	—	—	—	—	115/113
43	$0.80_{-0.08}^{+0.08}$	$2.35_{-0.10}^{+0.10}$	$58.9_{-5.1}^{+5.3}$	—	—	—	—	231/242
44	$0.79_{-0.10}^{+0.11}$	$2.46_{-0.13}^{+0.14}$	$18.5_{-2.8}^{+3.0}$	—	—	—	—	151/162
45	$0.64_{-0.12}^{+0.13}$	$2.19_{-0.15}^{+0.16}$	$27.1_{-3.7}^{+4.0}$	—	—	—	—	142/150
46	$0.55_{-0.11}^{+0.12}$	$2.24_{-0.15}^{+0.16}$	$16.7_{-2.9}^{+3.1}$	—	—	—	—	150/145
47	$0.52_{-0.10}^{+0.11}$	$2.47_{-0.18}^{+0.19}$	$13.8_{-2.4}^{+2.6}$	—	—	—	—	143/146
48	$0.44_{-0.08}^{+0.09}$	$2.32_{-0.14}^{+0.15}$	$21.6_{-2.8}^{+3.1}$	—	—	—	—	142/163
49	$0.43_{-0.10}^{+0.11}$	$2.33_{-0.17}^{+0.18}$	$13.0_{-2.1}^{+2.4}$	—	—	—	—	167/143
50	$0.49_{-0.12}^{+0.13}$	$2.78_{-0.24}^{+0.27}$	$6.1_{-1.3}^{+1.5}$	—	—	—	—	105/98
51	$0.84_{-0.10}^{+0.11}$	$2.14_{-0.11}^{+0.12}$	$16.8_{-3.0}^{+3.1}$	—	—	—	—	200/199
52	$0.83_{-0.06}^{+0.06}$	$2.25_{-0.06}^{+0.07}$	$128.4_{-7.8}^{+8.0}$	—	—	—	—	387/393
53	$0.90_{-0.09}^{+0.10}$	$2.38_{-0.11}^{+0.11}$	$41.5_{-4.1}^{+4.3}$	—	—	—	—	207/223
54	$0.92_{-0.11}^{+0.12}$	$2.31_{-0.12}^{+0.12}$	$25.1_{-2.9}^{+3.1}$	—	—	—	—	210/191
55	$0.99_{-0.11}^{+0.12}$	$2.06_{-0.10}^{+0.10}$	$54.6_{-5.0}^{+5.2}$	—	—	—	—	229/226
56	$0.49_{-0.10}^{+0.10}$	$2.07_{-0.13}^{+0.14}$	$27.5_{-4.0}^{+4.3}$	—	—	—	—	162/155
57	$0.54_{-0.11}^{+0.12}$	$2.35_{-0.17}^{+0.18}$	$10.7_{-1.8}^{+2.0}$	—	—	—	—	149/142
58	$0.40_{-0.06}^{+0.06}$	$2.46_{-0.11}^{+0.12}$	$23.6_{-2.6}^{+2.7}$	—	—	—	—	196/205
59	$1.10_{-0.12}^{+0.13}$	$2.33_{-0.12}^{+0.13}$	$47.4_{-4.7}^{+5.0}$	—	—	—	—	178/183
60	$0.98_{-0.08}^{+0.08}$	$2.46_{-0.09}^{+0.09}$	$41.1_{-3.5}^{+3.7}$	—	—	—	—	272/284
61	$1.14_{-0.10}^{+0.11}$	$2.50_{-0.11}^{+0.11}$	$41.3_{-3.8}^{+4.0}$	—	—	—	—	284/249
62	$1.55_{-0.14}^{+0.15}$	$2.29_{-0.10}^{+0.10}$	$55.8_{-4.8}^{+4.9}$	—	—	—	—	286/259
63	$0.95_{-0.12}^{+0.13}$	$2.19_{-0.12}^{+0.12}$	$42.7_{-4.2}^{+4.4}$	—	—	—	—	206/191
64	$0.54_{-0.06}^{+0.06}$	$2.29_{-0.08}^{+0.09}$	$47.1_{-4.1}^{+4.3}$	—	—	—	—	278/266
65	$0.32_{-0.06}^{+0.06}$	$2.49_{-0.12}^{+0.12}$	$22.7_{-2.6}^{+2.8}$	—	—	—	—	194/198
66	$0.84_{-0.13}^{+0.14}$	$2.36_{-0.14}^{+0.15}$	$21.3_{-2.8}^{+3.0}$	—	—	—	—	166/163
67	$1.36_{-0.11}^{+0.12}$	$2.46_{-0.10}^{+0.10}$	$53.7_{-4.4}^{+4.6}$	—	—	—	—	295/274
68	$1.99_{-0.18}^{+0.20}$	$2.36_{-0.11}^{+0.12}$	$64.1_{-5.2}^{+5.4}$	—	—	—	—	236/248
69	$1.69_{-0.28}^{+0.32}$	$2.26_{-0.18}^{+0.20}$	$30.2_{-3.8}^{+4.0}$	—	—	—	—	127/137
70	$0.33_{-0.10}^{+0.11}$	$2.01_{-0.17}^{+0.17}$	$13.3_{-2.3}^{+2.6}$	—	—	—	—	261/232

<sup>a</sup>The unit is  $10^{22} \text{ cm}^{-2}$ .

<sup>b</sup>The unit is  $10^{-8} \text{ erg s}^{-1} \text{ cm}^{-2} \text{ sr}^{-1}$ .

<sup>c</sup>The unit is keV.

<sup>d</sup>The unit is  $10^{17} \text{ cm}^{-5} \text{ sr}^{-1}$ .

<sup>e</sup>This region is excluded in our analysis and discussion due to a heavy contamination from a young SNR MCSNR J0536-6913 described well with a combination of non-thermal and NEI models.

(Wolk et al. 2002), Westerlund 1 (Muno et al. 2006) and IC 131 (Tüllmann et al. 2009). This sort of variation is observed also in SNRs and Nakamura et al. (2012) discussed the time evolution of the non-thermal component as a function of the radius which can be an indicator of the dynamical age of the SNR as described in Weaver et al. (1977). As an analogy of the SNR case, we also investigated the relation between the non-thermal luminosity and the radius of the SBs as shown in figure 6. The non-thermal luminosity goes up with increasing the radius up to  $\sim 40$  pc, whereas

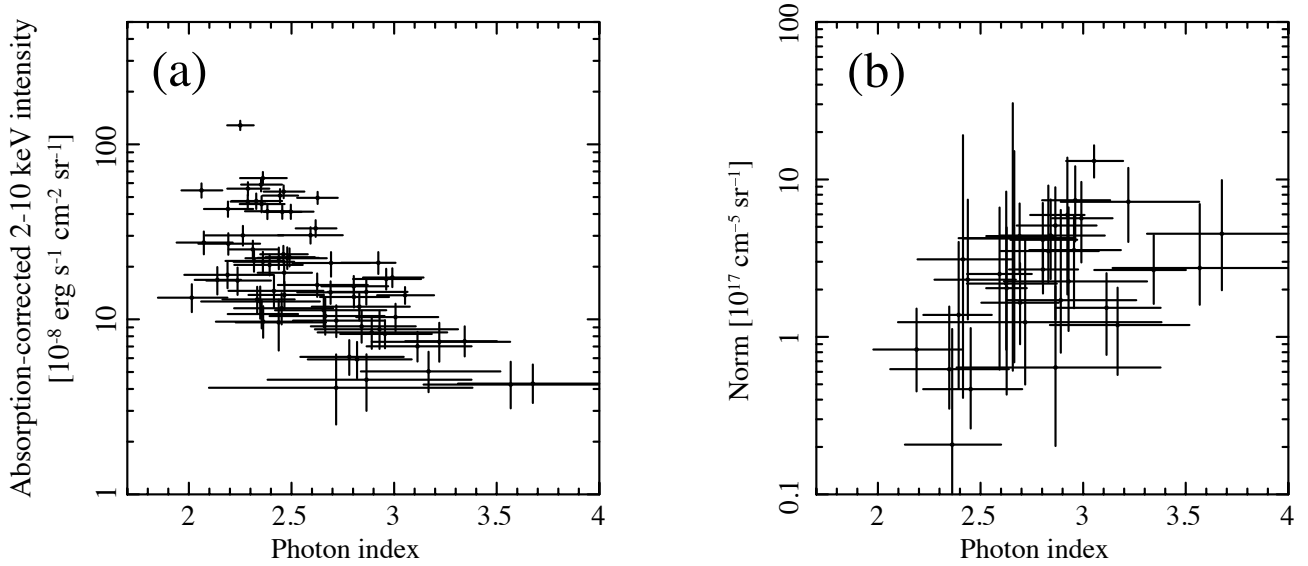


**Figure 5.** Correlation plots for (a) the photon index vs. the 2–10 keV intensity [ $10^{-8}$  erg s<sup>-1</sup> cm<sup>-2</sup>], (b) Normalization of the low temperature thermal components [ $10^{17}$  cm<sup>-5</sup> sr<sup>-1</sup>] vs. photon index, respectively.

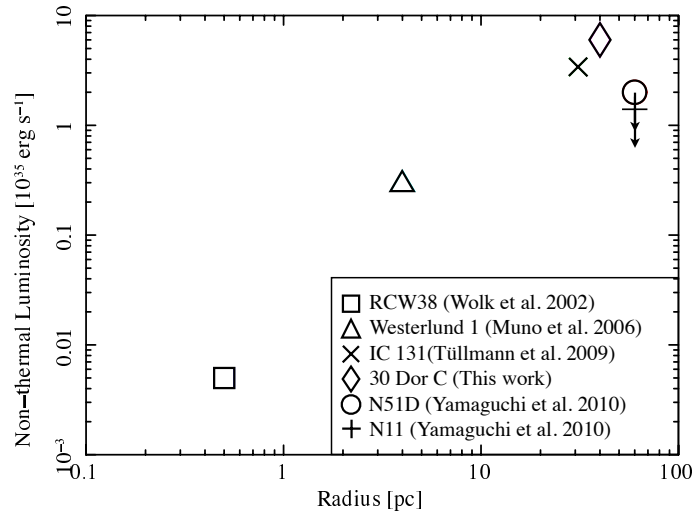


**Figure 6.** Non-thermal X-ray luminosity in 2–10 keV as a function of the radius for superbubbles.

it then appears to be decreases. 30 Dor C is located around the peak, which suggests that the system is currently on a phase of high energy particle acceleration.

## 5. SUMMARY

We conducted a detailed spatial analysis using the large amount of *XMM – Newton* archival data for 30 Dor C to study spatial variation of mainly the non-thermal component. The 30 Dor C field was divided into 70 regions with a physical scale of  $\sim 10$  pc and we found for the first time that the non-thermal emission exists in all the regions covering the whole field of 30 Dor C. The extracted spectra in the east region can be described well with a combination of the thermal and non-thermal models, whereas the spectra in the west region can be well fitted with the non-thermal model alone. The photon index and intensity in 2–10 keV indicate the spatial variation of  $\sim 2.0$ – $3.7$  and  $\sim (4$ – $130) \times 10^{-8}$  erg s<sup>-1</sup> cm<sup>-2</sup> str<sup>-1</sup>) in the field and the negative correlation between the non-thermal physical properties is

observed. The temperature and normalization of the thermal component also vary within a range of  $\sim 0.2\text{--}0.3$  keV and  $\sim 0.2\text{--}7 \times 10^{17}$  cm $^{-5}$  str $^{-1}$ , respectively. The positive correlation between the photon index and the normalization of the thermal component is also observed as is the case in SNRs, suggesting that the same acceleration mechanism dominates also in the superbubble.

This research was supported by a grant from the Hayakawa Satio Fund awarded by the Astronomical Society of Japan. HM is supported by JSPS KAKENHI Grand Number JP 15640356. IM acknowledge supports from the by JSPS KAKENHI Grand Number JP 26220703. HS is supported by JSPS KAKENHI Grand Number JP 16K17664. The authors are grateful to the anonymous referee for his/her comprehensive comments and useful suggestions, which improved the paper very much.

## REFERENCES

- Ackermann, M., Ajello, M., Allafort, A., et al. 2013, *Science*, 339, 807
- Anders, E., & Grevesse, N. 1989, *Geochim. Cosmochim. Acta*, 53, 197
- Bamba, A., Ueno, M., Nakajima, H., & Koyama, K. 2004, *ApJ*, 602, 257
- Bamba, A., Yamazaki, R., & Hiraga, J. S. 2005a, *ApJ*, 632, 294
- Bamba, A., Yamazaki, R., Yoshida, T., Terasawa, T., & Koyama, K. 2005b, *ApJ*, 621, 793
- Bruhweiler, F. C., Gull, T. R., Kafatos, M., & Sofia, S. 1980, *ApJ*, 238, L27
- Cooper, R. L., Guerrero, M. A., Chu, Y.-H., Chen, C.-H. R., & Dunne, B. C. 2004, *ApJ*, 605, 751
- Dickey, J. M., & Lockman, F. J. 1990, *ARA&A*, 28, 215
- Dunne, B. C., Points, S. D., & Chu, Y.-H. 2001, *ApJS*, 136, 119
- Inoue, T., Yamazaki, R., Inutsuka, S.-i., & Fukui, Y. 2012, *ApJ*, 744, 71
- Jansen, F., Lumb, D., Altieri, B., et al. 2001, *A&A*, 365, L1
- Kavanagh, P. J., Sasaki, M., Bozzetto, L. M., et al. 2015, *A&A*, 573, A73
- Koyama, K., Petre, R., Gotthelf, E. V., et al. 1995, *Nature*, 378, 255
- Kushino, A., Ishisaki, Y., Morita, U., et al. 2002, *PASJ*, 54, 327
- Le Marne, A. E. 1968, *MNRAS*, 139, 461
- Maddox, L. A., Williams, R. M., Dunne, B. C., & Chu, Y.-H. 2009, *ApJ*, 699, 911
- Muno, M. P., Law, C., Clark, J. S., et al. 2006, *ApJ*, 650, 203
- Nakamura, R., Bamba, A., Dotani, T., et al. 2012, *ApJ*, 746, 134
- Reynolds, S. P. 1998, *ApJ*, 493, 375
- Reynolds, S. P., & Keohane, J. W. 1999, *ApJ*, 525, 368
- Rothenflug, R., Ballet, J., Dubner, G., et al. 2004, *A&A*, 425, 121
- Russell, S. C., & Dopita, M. A. 1992, *ApJ*, 384, 508
- Sano, H., Fukuda, T., Yoshiike, S., et al. 2015, *ApJ*, 799, 175
- Sano, H., Yamane, Y., Voisin, F., et al. 2017, *ApJ*, 843, 61
- Sasaki, M., Haberl, F., & Pietsch, W. 2002, *A&A*, 392, 103
- Smith, D. A., & Wang, Q. D. 2004, *ApJ*, 611, 881
- Smith, R. K., Brickhouse, N. S., Liedahl, D. A., & Raymond, J. C. 2001, *ApJ*, 556, L91
- Someya, K., Bamba, A., & Ishida, M. 2014, *PASJ*, 66, 26
- Testor, G., Schild, H., & Lortet, M. C. 1993, *A&A*, 280, 426
- Tsubone, Y., Sawada, M., Bamba, A., Katsuda, S., & Vink, J. 2017, *ApJ*, 835, 34
- Tüllmann, R., Long, K. S., Pannuti, T. G., et al. 2009, *ApJ*, 707, 1361
- Weaver, R., McCray, R., Castor, J., Shapiro, P., & Moore, R. 1977, *ApJ*, 218, 377
- Wolk, S. J., Bourke, T. L., Smith, R. K., Spitzbart, B., & Alves, J. 2002, *ApJ*, 580, L161
- Yamaguchi, H., Bamba, A., & Koyama, K. 2009, *PASJ*, 61, S175
- Yamaguchi, H., Sawada, M., & Bamba, A. 2010, *ApJ*, 715, 412
- Yoshino, T., Mitsuda, K., Yamasaki, N. Y., et al. 2009, *PASJ*, 61, 805
- Zirakashvili, V. N., & Ptuskin, V. S. 2008, *ApJ*, 678, 939